

<https://doi.org/10.1038/s41529-025-00591-w>

Oxygen-driven shell-like microstructure: a pathway to high-performance PVD Cr coatings for metal protection



Meiqi Zhang^{1,2}, Li Wang¹, Zhenyu Wang¹✉, Yong Cheng^{1,2}, Guanshui Ma¹, Shiyao Tan^{1,2}, Peiling Ke^{1,3} & Aiyang Wang^{1,3}✉

Chromium (Cr) coatings, known for their corrosion resistance and luster, often suffer from coarse columnar grains when fabricated by physical vapor deposition (PVD), limiting their performance. This study employs high-power impulse magnetron sputtering (HiPIMS) with oxygen doping (8.3 at.%) to enhance Cr coatings on 316 L stainless steel. The optimized coating exhibits a unique shell-like microstructure, increasing hardness by 55% and improving crack resistance. Oxygen doping also reduces corrosion current density by over an order of magnitude, forming a continuous, low-defect amorphous passivation film for superior corrosion protection. This approach offers a simple yet effective strategy to advance Cr coating performance for industrial applications.

The surface of a material serves as the critical interface between the bulk material and its surrounding environment, playing a pivotal role in determining functional performance and durability^{1,2}. Chromium (Cr) coatings are widely employed in decorative applications due to their aesthetic appeal and dual functionality in wear and corrosion resistance^{3–6}, making them ideal for use in automobile parts, high-end bathroom fixtures, etc^{7,8}. Additionally, Cr coatings have been applied in the protection of accident-tolerant zirconium alloy cladding. In the initial stages, the primary production method for decorative Cr coatings relied on electroplating. However, traditional Cr plating faces significant challenges related to environmental impact and process sustainability^{9–11}. The search for electroplating alternatives has expanded to encompass a broad spectrum of surface modification technologies worldwide, ranging from electrochemical deposition and thermal spraying to advanced techniques like HVOF (high-velocity oxygen-fuel) spraying, cold spraying, and other novel deposition methods^{12,13}.

Recently, physical vapor deposition (PVD) technology has emerged as a superior alternative, gradually replacing electroplating as the preferred method^{14,15}. PVD offers numerous advantages, including low deposition temperatures, compatibility with diverse substrates, and the ability to produce smooth, dense coatings with precise compositional control. These features make PVD highly suitable for industrial-scale applications as a replacement for electroplating^{3,16,17}, despite its relatively higher equipment and operational costs compared to traditional methods. Current PVD technologies include magnetron sputtering and arc ion plating^{18–20}, with magnetron sputtering being the most widely adopted due to its superior control over coating quality^{16,21}.

High-power pulsed magnetron sputtering (HiPIMS) is a groundbreaking advancement in PVD technology, derived from conventional DC magnetron sputtering. Characterized by its highly ionized deposition process, HiPIMS has garnered significant attention in the materials research community and is widely recognized as a pivotal milestone in the development of PVD techniques^{22–24}. A comparative study by Zhang et al.²⁵ highlighted the superior performance of CrN coatings deposited via HiPIMS compared to those produced by conventional DC magnetron sputtering on ABS substrates. The HiPIMS-deposited CrN coatings exhibited a dense nanocrystalline structure with a prominent (200) texture, in contrast to the loose amorphous/nanocrystalline composite coatings observed in DC-mode deposits. This dense structure conferred exceptional corrosion resistance and mechanical properties to the HiPIMS-deposited coatings.

Further advancements in optimizing HiPIMS-deposited coatings were demonstrated by Kuo et al.²⁶, who revealed that synchronized pulsed biasing significantly enhances coating density. This technique intensifies Cr ion bombardment, effectively reducing defects and voids within the coating while improving its hardness. HiPIMS combined with synchronized pulsed biasing thus emerges as a cutting-edge method for producing high-performance Cr coatings, establishing a new benchmark in PVD-coated material performance²⁷. Cr coatings produced via PVD technology often suffer from penetrating columnar crystal defects, which compromise structural integrity and durability. To address this issue, multilayer composites are commonly employed to disrupt columnar crystal growth. However, the multilayer systems frequently involve heterogeneous

¹State Key Laboratory of Advanced Marine Materials, Ningbo Institute of Materials Technology and Engineering, Chinese Academy of Sciences, Ningbo, 315201, China. ²School of Materials Science and Chemical Engineering, Ningbo University, Ningbo, 315211 Zhejiang, China. ³Center of Materials Science and Optoelectronics Engineering, University of Chinese Academy of Sciences, Beijing, 100049, China. ✉e-mail: wangzy@nimte.ac.cn; aywang@nimte.ac.cn

interfaces²⁸ which can initiate galvanic coupling corrosion and other adverse effects^{29–32}.

Oxygen (O), one of the most abundant elements on Earth, readily introduces interstitial impurities or forms ceramic phases, such as oxide particles, within metallic matrices^{33–35}. Firstov et al.³⁶ developed the concept of “useful” impurities by doping metal coatings with oxygen, which allows one to obtain nanostructured materials with high hardness (strength) through grain boundary engineering. In a pioneering study, Lei et al.³⁷ demonstrated the formation of an ordered O composite in a TiZrHfNb high-entropy alloy bulk by incorporating O, significantly enhancing its room-temperature strength and toughness. Despite these advances, the mechanisms governing the high-temperature properties of high-entropy alloy coatings remain insufficiently understood. The crystal chemistry model proposed by Erdemir³⁸, along with research on Magnéli oxides, offers key insights into the behavior of oxides in metallic systems. According to the

model, the metal ion potential affects the cationic shielding effect of surrounding O ions. A higher metal ion potential facilitates the formation of O vacancies within the oxide microstructure, leading to a shear-susceptible structure. Such a phenomenon offers a novel pathway for manipulating O in metallic coatings to improve their mechanical and functional properties.

This study presents an innovative approach to Cr coating development by combining HiPIMS with synchronized pulsed bias and controlled oxygen doping (8.3 at.% O). Unlike previous studies focusing solely on either functional or decorative properties, our work achieves a breakthrough by simultaneously: (1) creating a unique shell-like microstructure through precise oxygen incorporation, (2) maintaining excellent decorative metallic luster, and (3) significantly enhancing both mechanical properties and corrosion resistance. Comparative analysis with undoped coatings demonstrates that oxygen performs dual functions: grain refinement and passive film formation. These findings enable a new approach to decorative coating design that overcomes limitations of traditional PVD and electroplating processes.

Results

Phase composition and microstructure

Figure 1 shows the XRD diffractograms of the Cr and Cr (8.3O) coatings for comparison. XRD analysis reveals significant differences in crystallographic orientation. The Cr (211) peak, observed in the pure Cr coating, disappears in the Cr (8.3O) coating, while the Cr (200) peak becomes more prominent. The strong Cr (110) peak in pure Cr also becomes weak after oxygen doping. Additionally, both Cr (100) and Cr (200) peaks exhibit significant broadening after O doping. This indicates that O doping promotes the preferential growth of the Cr (200) plane, inhibits the Cr (211) and Cr (110) planes, and reduces the grain size of the Cr coating. Furthermore, no Cr₂O₃ phase is detected in the XRD results, suggesting that the O doping content is relatively low and exists as a solid solution or that the amount of Cr₂O₃ formed is minimal and below the detection limit of XRD.

Figure 2 illustrates the surface and cross-sectional morphologies of the Cr and Cr (8.3O) coatings. The introduction of minor O doping leads to a clear transformation of the cross-sectional structure, from coarse columnar grains (Fig. 2a) to finer columnar granular structures (Fig. 2d). Simultaneously, the surface morphology shifts from a serrated structure (Fig. 2b) to a circular cauliflower-like appearance (Fig. 2e), indicating effective grain refinement induced by O doping. It is evident that O doping significantly

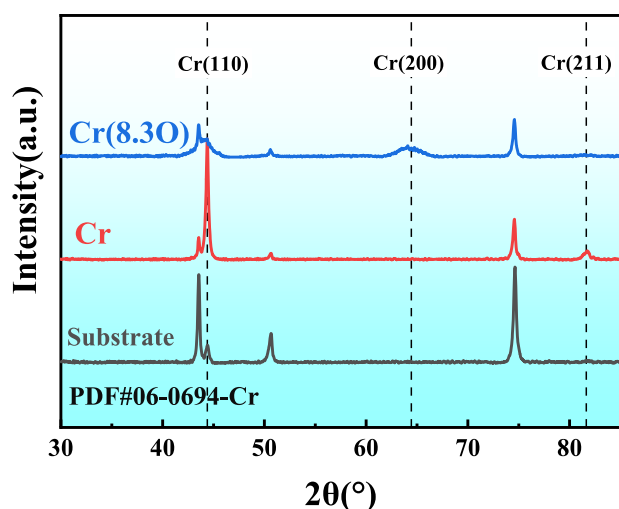


Fig. 1 | XRD patterns. The XRD patterns clearly exhibit characteristic peaks from the substrate (gray curve), Cr coating (red curve), and Cr (8.3O) coating (8.3 at.% O, blue curve), with reference diffraction peaks from standard Cr (PDF#06-0694) marked by black dashed lines for comparison.

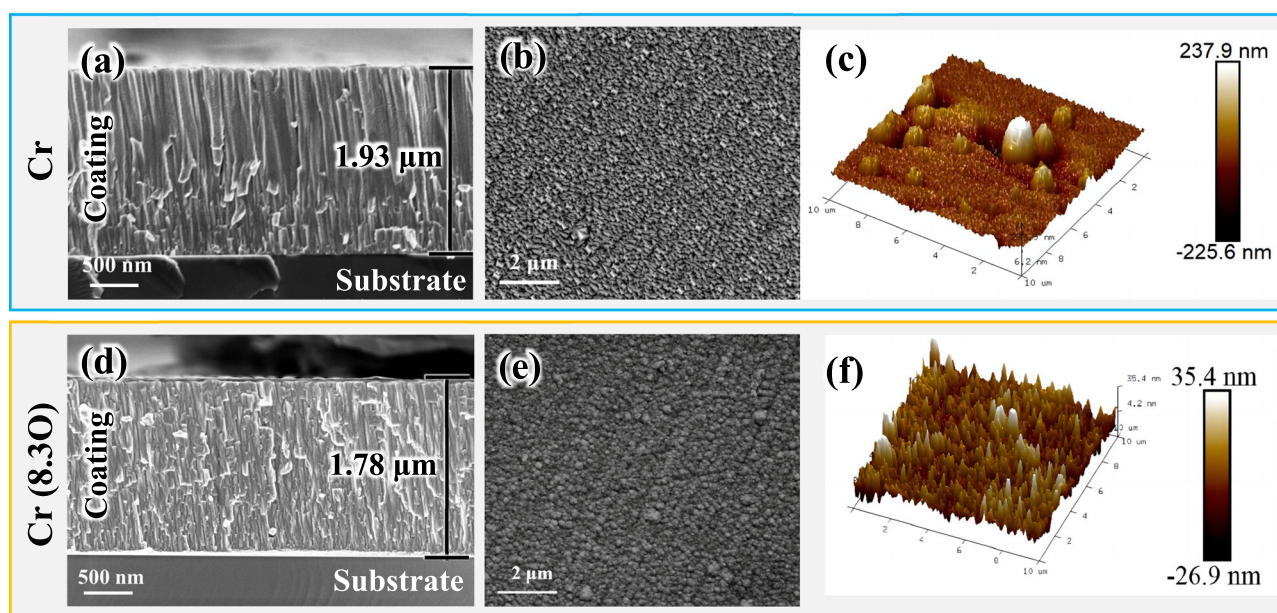


Fig. 2 | SEM and SPM morphology of the coatings. SEM cross-sectional (a, d) and surface morphology images (b, e), along with SPM three-dimensional surface topography images (c, f).

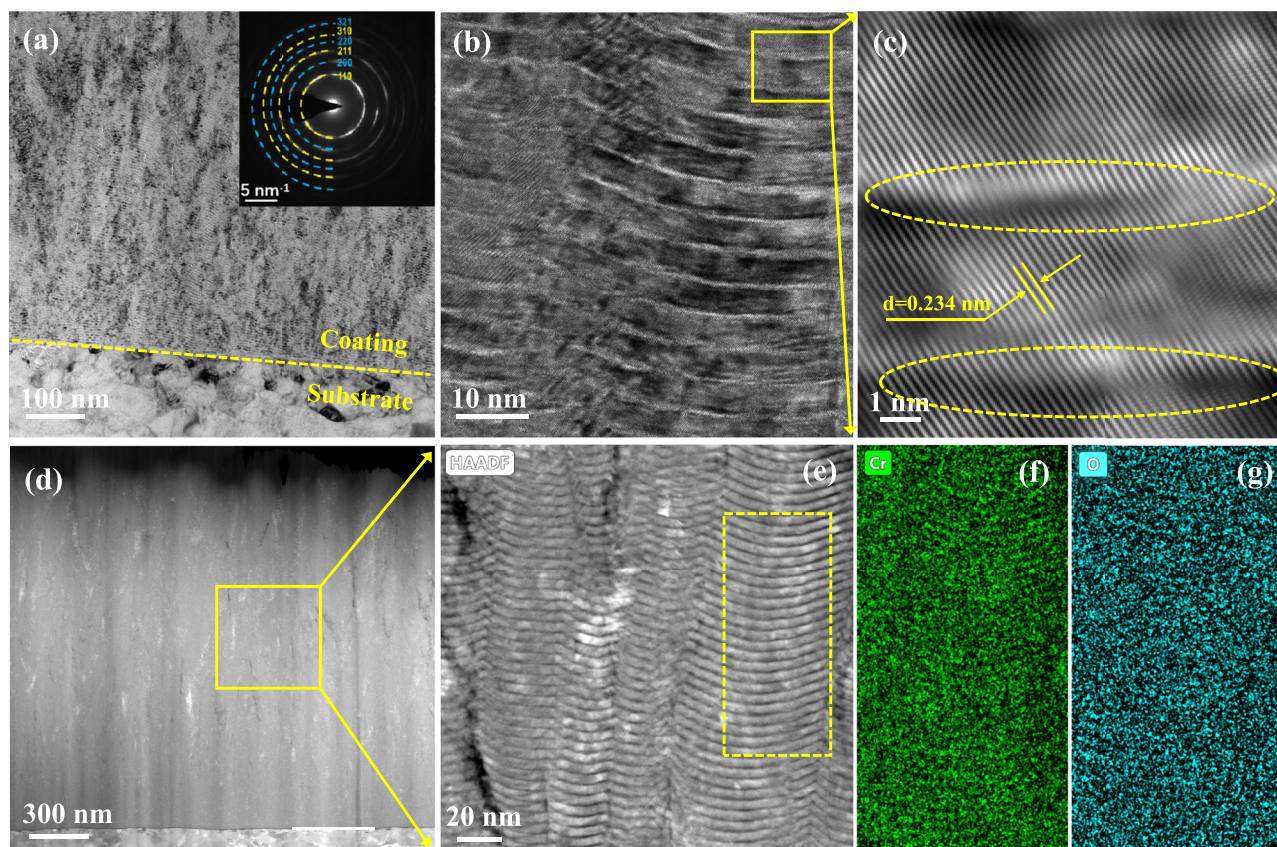


Fig. 3 | Cross-sectional TEM results of Cr (8.3O) coatings. (a) Bright-field phase and its SAED plot, (b, c) HRTEM and its STEM high-resolution results, (d–g) HAADF plots and its EDS results.

reduces the pores and other defects in the coating, leading to a marked improvement in its densification. Moreover, under identical deposition time, the coating thickness decreases by approximately 150 nm after O doping. This reduction is likely attributed to modified growth dynamics caused by O doping, which lowers the deposition rate by altering the nucleation and growth processes of the Cr coating. Surface topography analysis by SPM (Fig. 2c, f) further reveals a fivefold reduction in surface roughness (R_a) from 30.5 nm for the pure Cr coating to 6.1 nm for the Cr (8.3O) coating. This significant smoothing effect originates from oxygen's multifaceted role in modifying deposition kinetics: (1) The incorporation of oxygen element during HiPIMS deposition alters surface diffusion energetics, suppressing three-dimensional island growth that typically generates coarse features in pure Cr coatings; (2) Oxygen-induced nucleation of nanoscale Cr-O clusters promotes lateral growth uniformity through continuous enucleation events; (3) The resulting elimination of deep inter-columnar grooves (depth <50 nm in Cr(8.3O) vs. >200 nm in pure Cr) substantially reduces surface defect density. These synergistic effects not only produce exceptionally smooth surfaces but also critically minimize localized corrosion initiation sites, explaining the observed order-of-magnitude improvement in corrosion resistance (Fig. 6).

To further investigate the effect of O doping on the microstructure of the Cr coating, TEM was employed for detailed structural characterization, as shown in Fig. 3. As seen in Fig. 3a, the Cr (8.3O) coating exhibits a dense structure without distinct columnar grain features, in contrast to the typical columnar microstructure observed in the pure Cr coating²⁷. The absence of micro-voids, cracks, and large grain boundaries suggests that O doping refines the grains and disrupts the continuous growth of the columnar crystals. Selected area electron diffraction (SAED) results (inset of Fig. 3a) confirm that the coating retains the Cr phase, with no new phases introduced by O doping. High-magnification imaging of a local region (Fig. 3b) reveals a lamellar structure with alternating bright and dark layers, with the

bright layers approximately 1 nm thick. HRTEM (High-Resolution Transmission Electron Microscopy) analysis (Fig. 3c) of this region shows the Cr (200) orientation, where the presence of the bright layers distorts the Cr lattice fringes as designated by dotted circles in the figure, although the continuity of the lattice remains intact. Further STEM analysis (Fig. 3d, e) more clearly highlights the lamellar structure, which resembles a shell-like morphology, expected to enhance the strength and toughness of the coating.

Since contrast in STEM images is primarily related to element weight, dark regions correspond to lighter elements, in contrast to bright-field imaging. EDS mapping scan analysis (Fig. 3f, g) of the selected region (Fig. 3e) shows that the dark regions are depleted in Cr and enriched in O, while the bright regions are Cr-enriched. It is inferred that the formation of Cr-rich and O-rich regions is due to the rotation of the substrate holder. Due to the diffusion of gas throughout the chamber, when the substrate holder faces away from the target, the distribution of Cr is less concentrated. In contrast, O elements are more evenly distributed, as evidenced by the EDS results, where O is uniformly distributed, while Cr-rich regions form a laminated structure. The thickness of each shell-like layer (4–5 nm), the overall thickness of the coating, the deposition time, and the rotational speed of the base frame corroborate this conjecture.

Mechanical properties

The mechanical properties of the coating are closely linked to its microstructure and play a critical role in determining adhesion strength and service life. Fig. 4a presents the in-situ load-displacement curves obtained from nanoindentation testing of both coatings. The curves exhibit a smooth and consistent progression, devoid of any significant fluctuations and abrupt changes, which suggests the absence of internal defects within the coating. It is worth noting that the Cr (8.3O) coating requires a larger load to achieve the same indentation depth, which indicates that it has a higher hardness. Fig. 4b displays the hardness, elastic modulus, H/E ratio, and

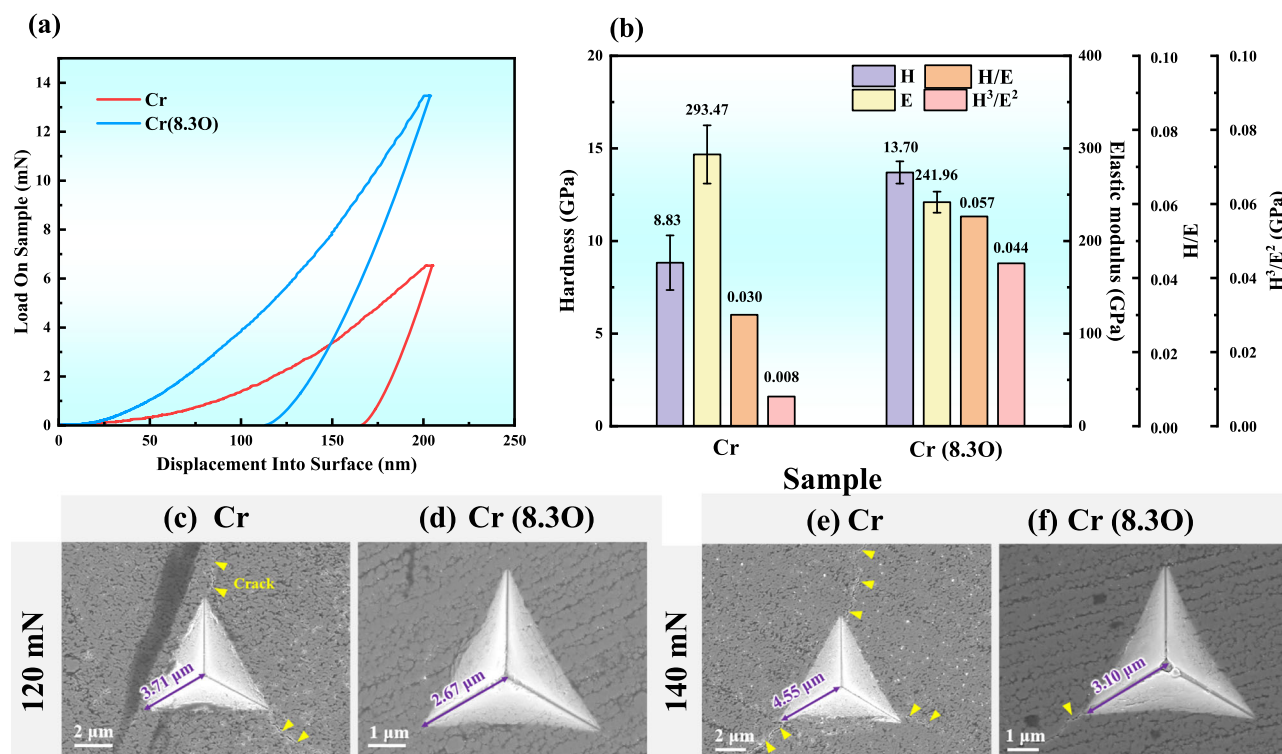


Fig. 4 | Nanoindentation testing of coatings. **a** Load-penetration depth curves of the coatings, **b** Hardness, modulus of elasticity, H/E , H^3/E^2 for both coatings; **(c–f)** SEM morphologies of Cube indentation under different loads.

H^3/E^2 ratio for both coatings. After O doping, the hardness of the coating increased from 8.83 GPa to 13.7 GPa, a 55.15% improvement; the elastic modulus decreased from 293.47 GPa to 241.96 GPa; the H/E ratio increased from 0.030 to 0.057, representing a 90% enhancement; and the H^3/E^2 ratio rose from 0.008 to 0.044, a remarkable 450% increase. A higher H/E and H^3/E^2 ratio can effectively prevent plastic deformation of the coating and mitigate rapid stress reduction within the coating, thereby enhancing its toughness. These improvements are attributed to the shell-like structure of the Cr (8.3O) coating, which significantly enhances both strength and toughness.

Figure 4c–f presents the SEM images of cube indentations under different loads. At a load of 120 mN, the Cr coating exhibits two cracks of varying lengths, while the Cr (8.3O) coating shows no visible cracks. When the load is increased to 140 mN, the number of cracks in the Cr coating continues to increase, whereas fine cracks begin to appear in the Cr (8.3O) coating. Notably, the indentation length in the Cr (8.3O) coating is significantly smaller than in the Cr coating, indicating superior hardness and toughness of the Cr (8.3O) coating, which aligns with the nanoindentation results. The main contributing factors include: (1) O doping increases coating density and refines the grain structure, leading to grain refinement strengthening; (2) The multi-interface structure of the shell-like coating effectively deflects crack propagation, while the strong interfacial bonding between layers prevents delamination or spalling, thereby enhancing the overall toughness of the coating.

Electrochemical corrosion properties

EIS tests were conducted on the coatings under stable open-circuit potentials, with the results presented in Fig. 5. Representative Nyquist and Bode plots reveal that the corrosion behavior of both coatings is similar, as evidenced by comparable curve shapes. In the Nyquist plot (Fig. 5a), both samples display an incomplete capacitive loop across the entire tested frequency range, indicating distinct capacitive reactance. This suggests that the electrode reaction is primarily governed by electrochemical processes³⁹. The radius of the capacitive reactance arc reflects the passivation film impedance

and interfacial charge transfer resistance. A larger arc radius typically indicates higher passivation film impedance, which hinders charge transfer and migration, thereby enhancing corrosion resistance⁴⁰. Following O doping, the radius of the capacitive reactance arc increases significantly, indicating improved passivation film properties. The Bode plot (Fig. 5b) reveals distinct frequency-dependent behavior, with the high-frequency region showing a phase angle approaching 0° and frequency-independent impedance modulus, clearly indicating dominant resistive behavior governed by the electrolyte solution resistance (R_s). Compared to Cr coating, the Cr (8.3O) coating demonstrates significantly improved electrochemical characteristics at medium and low frequencies, maintaining a consistently high phase angle and a greater impedance modulus. These quantitative differences unambiguously demonstrate that the oxygen-doped coating forms a passive film with superior dielectric properties and corrosion resistance, attributed to its more homogeneous and defect-resistant structure. These findings highlight that the O-doped coating offers superior protective performance for the SS316 substrate.

In this model, R_s , R_p , and R_{ct} represent the solution resistance, the pore resistance, and the charge interfacial transfer resistance of the coating, respectively. Given that the impedance plots of both coatings exhibit similar shapes, the same equivalent circuit model, $R(Q(R(QR)))$, was selected (illustrated in the inset of Fig. 5a). The fitting results are provided in Table 1. The impedance data, fitted using this model (solid lines), show excellent agreement with the measured data (scattered points), with the chi-squared values (χ^2) on the order of 10^{-5} , indicating that the selected equivalent circuit accurately reflects the electrochemical corrosion behavior of the samples in a 3.5 wt% NaCl solution. In this model, R_s , R_p , and R_{ct} represent the solution resistance, the pore resistance of the coating, and the charge transfer resistance at the substrate surface, respectively. The R_{ct} value is commonly used to evaluate the resistance to the electrode reaction at the interface. A higher R_{ct} value indicates greater resistance to charge transfer and a slower corrosion rate⁴¹. The R_{ct} value of coating Cr (8.3O) is two orders of magnitude higher than that of Cr coating, indicating that the passivation film on the Cr (8.3O) coating significantly inhibits the charge transfer process, resulting in

Fig. 5 | EIS plots of the substrate and coatings.
(a) Nyquist plots. (b) Bode plots.

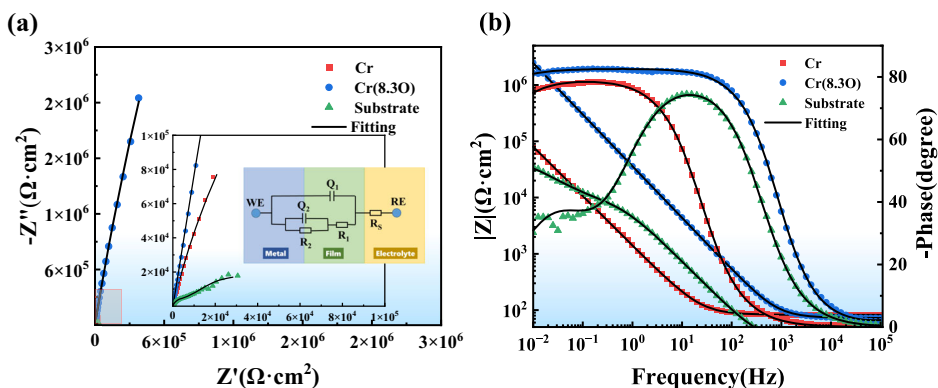


Table 1 | Fitted parameters from the equivalent circuits

Samples	Cr	Cr (8.3O)
$R_s(\Omega)$	86.0	100.0
$CPE_{po}(F \cdot cm^{-2})$	1.702×10^{-4}	6.219×10^{-8}
n_{po}	0.842	0.664
$R_{po}(\Omega)$	8.082×10^4	73.44
$CPE_{dl}(F \cdot cm^{-2})$	5.480×10^{-4}	5.071×10^{-6}
n_{dl}	0.800	0.921
$R_{ct}(\Omega)$	1.026×10^6	1.12×10^8
χ^2	3.515×10^{-5}	9.479×10^{-5}

a lower corrosion rate. The EIS results demonstrate that the Cr (8.3O) coating, with its more uniform and dense passivation film, effectively blocks the penetration of corrosive ions, significantly enhancing the corrosion resistance of the substrate in a 3.5 wt% NaCl solution.

Figure 6a shows the potentiodynamic polarization curves of the substrate and coatings in a 3.5 wt% NaCl solution. The electrochemical parameters, obtained through Tafel extrapolation fitting of the polarization curves, along with the parameters for the 316 L stainless steel substrate (range of -0.4 to $+0.4$ V vs. SCE), are summarized in Table 2. The polarization resistance (R_p) of each sample was calculated using the Stern-Geary Eq. (1)⁴²:

$$R_p = -\frac{\beta_a \beta_c}{2.303 i_{corr} (\beta_a \beta_c) A} \quad (1)$$

where β_a and β_c are the anodic and cathodic Tafel polarization slopes, respectively; i_{corr} is the corrosion current density; and A (0.2826 cm^2 in this study) represents the exposed area of all samples during testing. The anodic β_a values exceeding the cathodic β_c values for both coatings indicate that the corrosion process is primarily anodic in nature⁴³. The incorporation of O plasma significantly enhances corrosion resistance, resulting in a tenfold reduction in i_{corr} and a more than 35-fold increase in polarization resistance (R_p). These improvements highlight the effectiveness of O doping in reducing corrosion susceptibility. Assessing porosity is critical for evaluating the overall performance of the coating. The protection efficiency (P_e) and porosity (P_p) of the three samples were calculated using the following empirical Eqs. (2), (3)^{44–46}:

$$P_e = 100 \left(1 - \frac{i_{corr}}{i_{corr}^0} \right) \quad (2)$$

$$P_p = \left(\frac{R_{p(substrate)}}{R_{p(coating)}} \right) 10^{\left(-\frac{|\Delta E|}{\beta_a} \right)} \quad (3)$$

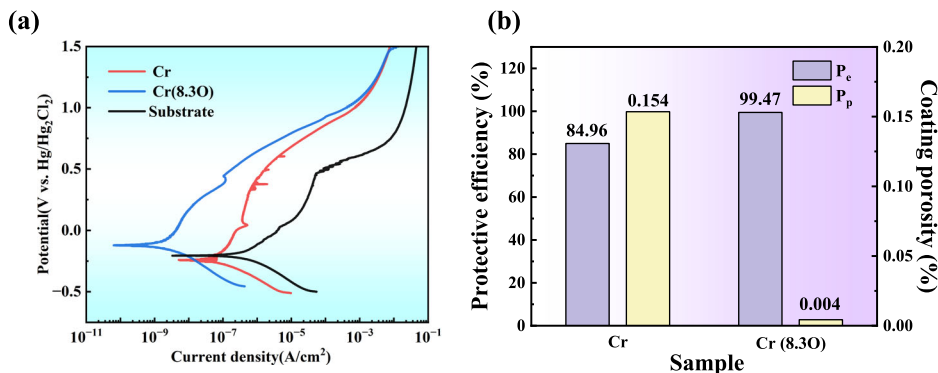
In this study, i_{corr} and i_{corr}^0 denote the corrosion current densities with and without the coating, respectively. R_p (substrate) and R_p (coating) represent the polarization resistances of the substrate and the coated sample, while $|\Delta E|$ refers to the absolute difference in the self-corrosion potentials between the coated specimen and the substrate. β_a is the slope of the anodic polarization curve of the substrate. The calculated results for the two coatings, shown in Fig. 6b, reveal that the O-doped coating achieves exceptionally high protection efficiency (approaching 100%) and extremely low porosity (approaching 0%). Overall, these findings indicate a significant enhancement in the coating's resistance to electrochemical corrosion.

To reveal the formation process, corrosion resistance, and mechanisms of the passivation film in a corrosive environment, both coatings were polarized at a constant potential of 0.4 V (vs. SCE) for 6 h. The constant potential polarization curve (Fig. 7a) shows a sharp increase in corrosion current density for the pure Cr coating after 2 h polarization, while the Cr (8.3O) coating maintains a stable and low corrosion current density throughout the 6 h test. A closer inspection of the first 4 h (Fig. 7b) shows that, within the initial 2 h, the corrosion current density of the Cr coating is significantly higher than that of the Cr (8.3O) coating, with noticeable fluctuations early on, indicating ongoing dissolution. Surface morphology analysis after corrosion shows that the Cr coating is severely damaged, with cracks and fragmentation observed (Fig. 7c), while the Cr (8.3O) coating remains largely intact (Fig. 7d). These findings conclusively demonstrate that the Cr (8.3O) coating exhibits superior electrochemical corrosion resistance compared to the pure Cr coating, highlighting its enhanced stability and protective performance.

XPS depth profiling was used to analyze the composition of the passivation films on both coatings, examining the variations in Fe (substrate element), Cr, and O content with etching time (Fig. 7e). The results show that after corrosion testing, the Fe content detected on the Cr coating surface is higher than the Cr content. This phenomenon is attributed to the corrosion-induced exposure of the substrate material, as the prolonged electrochemical testing caused progressive degradation of the Cr coating, allowing XPS analysis to detect the underlying substrate. Additionally, the O content in the Cr coating is higher than in the Cr (8.3O) coating, further indicating more severe corrosion of the Cr coating. In contrast, the Cr (8.3O) coating shows a higher surface O concentration before etching, likely due to O adsorption from exposure to air. After 30 s etching, the passivation film formed during constant potential polarization becomes distinctly visible. As etching progresses, the O concentration gradient diminishes, while Cr content increases and stabilizes after 300 s etching. Notably, no Fe was detected in the Cr (8.3O) coating, underscoring its superior protective barrier capability, which effectively prevents the diffusion of substrate elements.

TEM was employed to further analyze the structure and composition of the passivation film on the Cr (8.3O) coating. As shown in Fig. 7f, the passivation film is continuous and dense, with a distinct interface between the coating and the passivation film. The film thickness is approximately

Fig. 6 | Potentiodynamic polarization test and results. (a) Potentiodynamic polarization curves for the substrate and coatings. (b) Computed results for protection efficiency and porosity.



8–10 nm. Figure 7g reveals that the passivation film exhibits an amorphous structure, primarily attributed to the incorporation of O into the Cr coating, which induces rapid oxidation of Cr during polarization, leading to the formation of a dense passivation film. The migration and diffusion of atoms are markedly restricted, thereby inhibiting the formation of ordered structures or crystalline phases. The passivation film is also easily distinguishable in the STEM results (Fig. 7h). Composition analysis shows that the O content at location 2# in Fig. 7h is higher than that at location 1#, within the coating, with the Cr:O atomic ratio approaching 2:3, indicating that the passivation film is predominantly amorphous Cr₂O₃.

Passivation films are widely recognized as degenerate, heavily doped semiconductor layers. Variations in their composition and structure can significantly influence their semiconductor properties, depending on the type and concentration of dopants. Such variations are critical in determining the formation, breakdown, and pitting corrosion behavior of the Passivation films. Therefore, a comprehensive investigation of the semiconductor characteristics of passivation films is essential for understanding the fundamental electrochemical corrosion mechanisms of materials. The charge distribution at the film/electrolyte interface can be analyzed by examining the capacitance of the space charge region (C_{sc}) as a function of electrode potential (E), described by the Mott-Schottky equation⁴⁷:

For an n-type semiconductor (4):

$$\frac{1}{C_{sc}^2} = \frac{2}{\epsilon \epsilon_0 e N_D} \left(E - E_{fb} - \frac{kT}{e} \right) \quad (4)$$

For a p-type semiconductor (5):

$$\frac{1}{C_{sc}^2} = \frac{-2}{\epsilon \epsilon_0 e N_A} \left(E - E_{fb} - \frac{kT}{e} \right) \quad (5)$$

Here, ϵ , is the dielectric constant of the passivation film (typically 30 for Cr₂O₃)⁴⁸, and ϵ_0 is the vacuum permittivity (8.85×10^{-14} F/cm). e is the elementary charge (1.602×10^{-19} C), N_D and N_A represent donor and acceptor densities, respectively, and E_{fb} is the flat-band potential. The Boltzmann constant (k) is 1.38×10^{-23} J/K, and T is the absolute temperature (298 K). The slope of the Mott-Schottky plot is crucial for determining the charge carrier type and concentration in the passivation film, providing insight into its semiconductor behavior and its role in corrosion resistance.

Figure 8a presents the Mott-Schottky curves of passivation films formed after constant potential polarization of both coatings at +0.4 V (vs. stable E_{ocp}) in a 3.5 wt.% NaCl solution. To prevent substrate interference, the Cr coating was polarized for 2 h, while the Cr (8.3O) coating was polarized for 6 h. The results indicate that the passivation film formed on the Cr coating exhibits p-type semiconductor behavior within the negative potential range (−1.6 V to −0.6 V), suggesting the presence of Cr vacancies or acceptor-type defects, resulting in a high concentration of hole carriers. Two factors likely contribute to this behavior: (1) XPS analysis (Fig. 8e)

Table 2 | Tafel fitting parameters of potentiodynamic polarization curves

Sample	E_{corr} (V _{vs SCE})	$i_{corr} \cdot 10^{-8}$ (A·cm ⁻²)	β_a (mV/dec)	β_c (mV/dec)	R_p (mΩ·cm ²)
Cr	−0.2450	8.39	518.9	−118.3	0.499
Cr (8.3O)	−0.1210	0.298	641.5	−149.3	17.647
Sustrate	−0.2050	55.8	253.4	−159	0.076

indicates significantly higher O content in the passivation film of the Cr coating compared to the Cr (8.3O) coating, suggesting a composition closer to Cr₂O₃. The formation of Cr vacancies, high-valence Cr ions (>+3), or other defects acts as acceptor sites, facilitating hole conduction. (2) Chloride ions (Cl[−]) promote the dissolution or complexation of Cr ions (e.g., Cr³⁺ forming soluble complexes), thereby increasing the Cr vacancy concentration within the passivation film.

In contrast, the passivation film on the Cr (8.3O) coating exhibits n-type behavior between −1.2 V and −0.4 V, attributed to O vacancies or donor-type defects. The denser passivation film structure inhibits complete oxidation of Cr, resulting in a higher concentration of O vacancies. Upon increasing the potential (−0.4 V to 0 V), the passivation film transformed into p-type behavior, suggesting defect reconstruction or multiphase evolution, with a shift from donor-type defects (O vacancy-rich) to acceptor-type defects (Cr vacancy-rich) or higher-valence Cr states.

According to the Mott-Schottky equation, the carrier concentration information of the passivation film can be calculated from the slope of the straight line in Mott-Schottky plot (Fig. 8b). Generally, a higher carrier concentration in the passivation film correlates with increased instability and electrical conductivity, indicating a higher density of defects within the film. The carrier concentration N_A of the Cr (8.3O) coating is significantly lower than that of the Cr coating, suggesting that O doping facilitates the rapid formation of a more stable and protective passivation film.

Electrochemical corrosion mechanism

The above study established the influence of O doping on the micro-structure, mechanical properties, and corrosion resistance of Cr coatings. Figure 9 illustrates the schematic of the electrochemical corrosion mechanism for the Cr and Cr (8.3O) coatings. The relatively poor electrochemical corrosion resistance of the Cr coating can be attributed to two primary factors: (1) The presence of through-thickness columnar grain structures facilitates the rapid diffusion of chloride ions (Cl[−]) into the coating through grain boundary defects. This results in a high concentration of Cl[−] ions within the coating, which directly contacts the substrate, inducing electrochemical corrosion. (2) The Cr coating relies on a chromium oxide (Cr₂O₃) passivation film for protection. However, the relatively high surface roughness of the Cr coating ($R_a = 30.5$ nm), combined with the porosity and defects in the loose columnar grain structure, can cause local discontinuities or weak spots in the Cr₂O₃ passivation film. These areas,

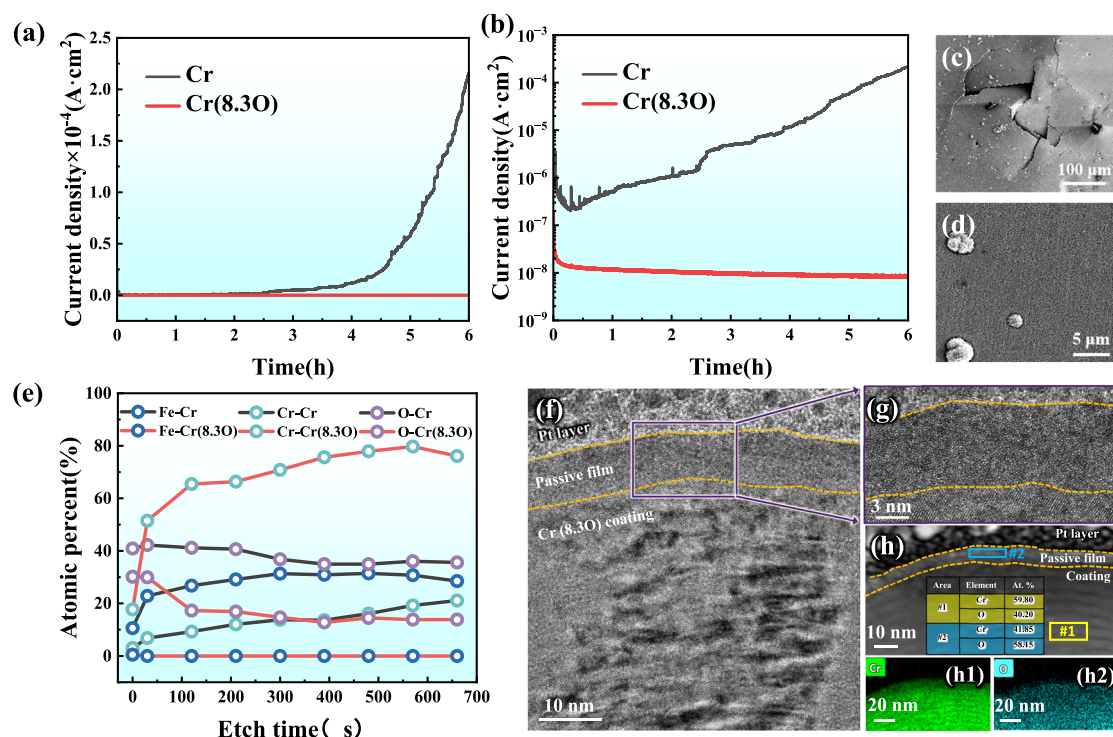
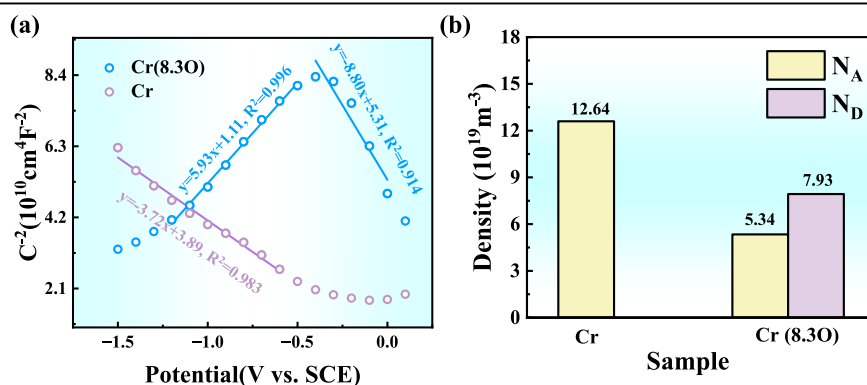


Fig. 7 | Passivation film characterization of Cr(8.3O) coating. (a) Potentiostatic polarization curves for the two coatings, (b) Potentiostatic polarization curves for the two coatings in log scale; (c) SEM surface appearances of the Cr coating after polarization; (d) SEM surface appearances of the Cr(8.3O) coating following

polarization; (e) The elemental composition varies with etching time; TEM results of the cross-section of the passivated Cr(8.3O) coating: (f, g) HRTEM and its enlarged image, (h) STEM images and their EDS results.

Fig. 8 | Mott-Schottky measurements of coatings. Mott-Schottky plot (a) and carrier density (b) of the passivation film developed on the coating following potentiostatic polarization at +0.4 V in a 3.5 wt% NaCl solution.



characterized by a higher carrier concentration, compromise its protective efficiency.

O doping modifies the structure of the Cr coating, resulting in a shell-like layered structure in the Cr (8.3O) coating, with alternating Cr-rich and Cr-lean layers. This unique structure imparts exceptional electrochemical corrosion resistance to the coating. On one hand, the dense structure effectively prevents the penetration of corrosive particles, providing a durable physical barrier to protect the substrate from corrosion. On the other hand, the dense structure promotes the continuity of the Cr_2O_3 passivation film, enhancing its stability and corrosion resistance⁴⁹. The smooth surface of the coating ($R_a = 6.1 \text{ nm}$) further reduces local potential differences, minimizing the formation of micro-galvanic cells and preventing localized corrosion. Additionally, the formed Cr_2O_3 passivation film exhibits an amorphous structure, which, due to the absence of grain boundaries and long-range order, possesses higher density and uniformity⁵⁰. Mott-Schottky analysis also confirms that the passivation film of Cr (8.3O) coating has a

lower carrier density, allowing it to effectively block the penetration of corrosive media (Cl^-) and provide superior protective performance.

Discussion

In this work, an innovative strategy was employed to significantly enhance the comprehensive performance of Cr coatings by introducing 8.3 at.% oxygen doping. Structural characterization revealed that the incorporation of oxygen induced a remarkable morphological transformation, evolving from a conventional continuous columnar grain structure to a unique shell-like architecture. This structural reorganization reduced surface roughness by 400%. Mechanical property tests demonstrated that the modified Cr (8.3O) coating exhibited a 55.15% increase in hardness (H), while the elastic modulus ratio (H/E) and the resistance to plastic deformation index (H^3/E^2) improved by 90% and 450%, respectively, indicating superior crack propagation resistance. Electrochemical impedance spectroscopy confirmed that the Cr (8.3O) coating displayed a larger capacitive arc radius, higher

Fig. 9 | Mechanism diagram of electrochemical corrosion of two coatings. The tests were performed in a 3.5 wt.% NaCl solution, corresponding to the pH value of around 7.

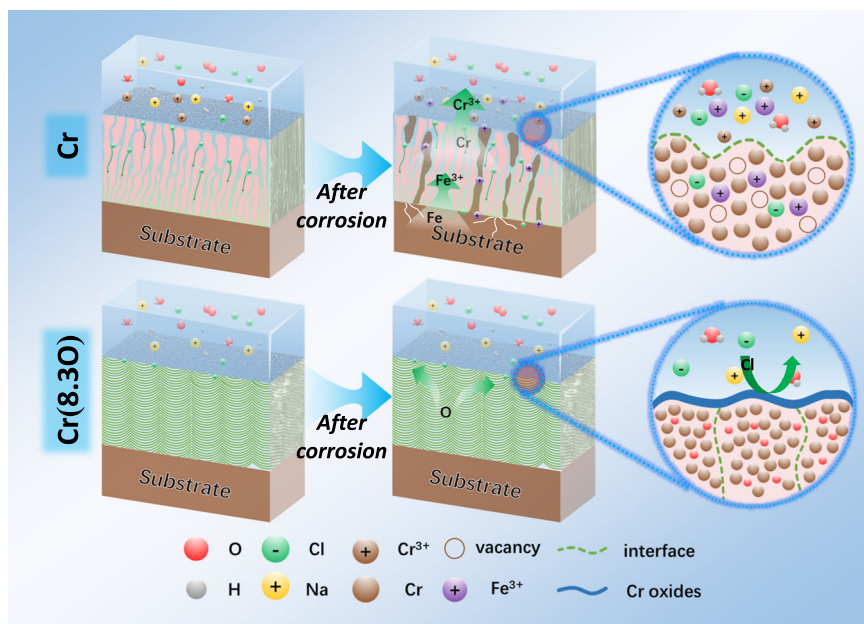
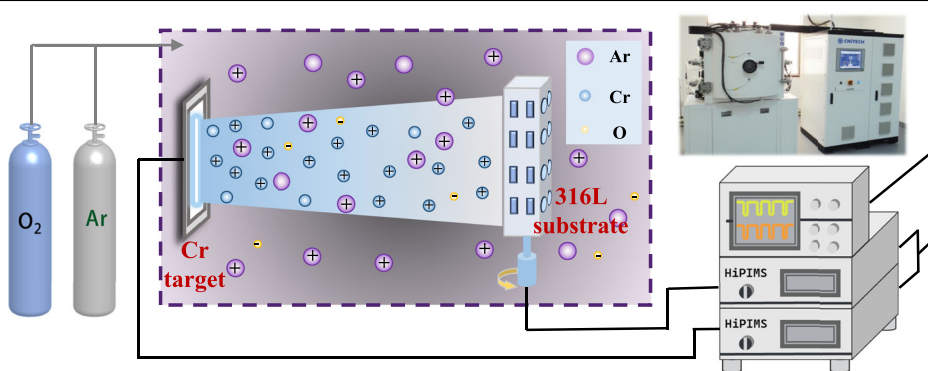


Fig. 10 | HiPIMS synchronized pulse biasing equipment and coating deposition process. The target and substrate bias were both connected to HiPIMS power supplies.



phase angle, and increased impedance modulus in the medium-to-low frequency range. Potentiodynamic polarization tests revealed a significant reduction in both corrosion current density and porosity. Notably, during a 6 h potentiostatic polarization test, the Cr (8.3O) coating exhibited exceptional stability, attributed to the formation of a highly dense, low-defect amorphous passive film that effectively suppressed charge transfer. In contrast, the undoped pure Cr coating failed after only 2.5 h. This study provides new insights and experimental evidence for developing Cr-based coatings with outstanding mechanical properties and long-term corrosion resistance.

Methods

Coating deposition

Cr coatings were fabricated using magnetron sputtering equipment, with both the target and bias power supplies operated by HiPIMS power sources. The target material was a pure metal Cr target (purity 99.99%), while Ar (purity 99.99%) and O (purity 99.99%) were used as the working gas. Commercially available 316 L austenitic stainless steel was used as substrates ($10 \times 10 \times 2 \text{ mm}^3$). Following mechanical polishing, the samples underwent sequential ultrasonic cleaning in acetone and ethanol. These prepared substrates were then characterized by surface morphology analysis, XRD, mechanical testing, and electrochemical measurements.

Figure 10 illustrates the HiPIMS synchronized pulsed bias system and the coating deposition process. After polishing and cleaning, the substrates

were fixed onto the base frame of the coating equipment and rotated at a constant speed of 4 rpm during deposition. The chamber vacuum was reduced to below $4.0 \times 10^{-3} \text{ Pa}$, after which Ar was introduced. To improve the adhesion, plasma etching was performed using Ar^+ ions generated by a linear anode layer ion source to remove surface impurities and oxides. During etching, the pressure was 0.2 Pa, the bias voltage was -100 V , the ion source current was 0.2 A, and the etching time was 30 min. Cr coatings were subsequently deposited with a target-substrate distance of 12 cm. The deposition parameters included an Ar flow rate of 50 sccm, an average HiPIMS power of 2984 W, a discharge voltage of 574 V, and a peak current of 5.2 A. Synchronized pulsed biasing was achieved via a signal generator, aligning the target discharge and bias waveforms. The substrate bias voltage was maintained at -80 V . Two types of coatings were prepared: pure Cr and Cr doped with a small amount of O. Deposition was conducted at room temperature without additional heating. Detailed deposition parameters are summarized in Table 3.

Coating characterization

The elemental composition and content of the coatings were analyzed using electron probe microanalysis (EPMA, JXA-iHP200F, JEOL, Japan). The detailed results of the analyses are listed in Table 2. The pure Cr coating had a Cr atomic percentage of 98.38 at.% with trace amounts of O impurities, whereas the O-doped Cr coating, designated as Cr (8.3O), contained 91.27 at.% Cr and 8.30 at.% O.

Table 3 | Deposition parameters of Cr (O) composite coatings prepared by HiPIMS

Sample	Duty cycle (%)	Gas flow (sccm)	Discharge voltage (V)	Operating current (A)	Average power (kW)	Power frequency (Hz)	Bias voltage (V)	Deposition time (h)	Element (at.%)	
									Cr	O
Cr	5	Ar/50	820	4	3	500	−80	1.5	98.38	1.62
Cr (8.3O)	5	Ar/50 O/3	820	4	3	500	−80	1.5	91.27	8.30

Surface and cross-sectional morphologies were characterized using field emission scanning electron microscopes (FE-SEM, Quanta 250 FEG, FEI, USA; S-4800, Hitachi, Japan) operating at 15 and 4 kV, respectively, with magnifications from 100× to 50000×. Energy-Dispersive X-Ray Spectroscopy (EDS) attached to the SEM was used for local chemical composition analysis. Three-dimensional surface morphology and roughness were measured using scanning probe microscopy (SPM, 3100 SPM).

Phase composition and crystal structure were investigated using X-ray diffraction (XRD, D8 Discover, Bruker, Germany) with Cu K α radiation ($\lambda = 0.1540$ nm). Scans were conducted from 5° to 90° with a step size of 0.02°, and patterns were analyzed using Jade 6.0 software. Depth-resolved elemental analysis was performed using X-ray photoelectron spectroscopy (XPS, Axis Ultra DLD, Kratos, UK) with monochromatic Al K α radiation ($h\nu = 1486.7$ eV). Microstructural analysis of coatings and surface oxides was carried out using transmission electron microscopy (TEM, Talos F200x, Thermo Fisher Scientific, USA) at 200 kV with a point resolution of 0.25 nm. TEM samples were prepared using focused ion beam (FIB, Auriga, Zeiss, Germany) milling, employing a liquid gallium ion source to mill regions of interest.

Mechanical and electrochemical corrosion tests

The hardness (H), elastic modulus (E) and fracture toughness (K_{IC}) of the coatings were evaluated using a nanoindenter (MTS NANO G200, USA) equipped with Berkovich and cube corner indenters. The Berkovich indenter (tip angle = 70.32°, radius = 30 nm) was used to measure hardness and modulus when the indentation depth was less than 1/10 of the coating thickness. The sharper cube corner indenter (tip angle = 35.26°, radius = 20 nm) was utilized for fracture toughness measurements due to its propensity for inducing coating damage under load.

Electrochemical corrosion performance was tested using a three-electrode setup with a Reference 600+ electrochemical workstation (Gamry Instruments, USA). The coated sample served as the working electrode (WE), a platinum wire as the counter electrode (CE), and a saturated calomel electrode (SCE) as the reference electrode (RE). The exposed area of the sample was standardized to 0.2 cm², and tests were performed in a 3.5 wt% NaCl solution, corresponding to the pH value of around 7. Before the electrochemical experiment, each test specimen underwent an open circuit potential (OCP) measurement with 10 min duration, followed by 5 min of cathodic polarization at 0.8 V vs. the initial E_{OCP} . The purpose was to reduce the air-formed oxide on the sample surface and stabilize the initial surface conditions. Similar treatment has been previously reported^{51,52}. Subsequently, a stable open circuit potential value was usually achieved after continuous immersion for 60 min. The potentiodynamic polarization curves were recorded from 0.50 to +1.50 V vs. the stable E_{OCP} with a scan rate of 1 mV s^{−1}. The potentiostatic polarization test was measured for 6 h at 0.4 V vs E_{OCP} . The electrochemical impedance spectroscopy (EIS) tests were conducted at a perturbing AC amplitude of 10 mV and scanning frequencies of 10⁵–10^{−2} Hz. The obtained EIS data were analyzed using the ZsimpWin software to fit the measured data numerically, which was available for the establishment of equivalent electric circuits (EEC). Moreover, the Mott-Schottky measurements were conducted on the passive films at a

fixed frequency of 1 kHz by performing a potential scan towards the negative direction with steps of 100 mV. All tests were repeated in the same conditions at least three times to confirm the experimental reproducibility. The most representative results were used for discussion in the present study.

Data availability

The data that support the findings of this study are available from the corresponding author upon reasonable request.

Received: 11 February 2025; Accepted: 21 April 2025;

Published online: 13 May 2025

References

1. Safavi, M. S., Ghazijahani, S. S. & Rasooli, A. Pulsed electroplating of ZrO₂-reinforced Ni-Cr alloy coatings from the duplex complexing agents-containing bath for engineering applications: Importance of operating conditions. *Heliyon* **10**, e37631 (2024).
2. Mozetič, M. Surface modification to improve properties of materials. *Materials* **12**, 441 (2019).
3. Ponte, F., Sharma, P., Figueiredo, N. M., Ferreira, J. & Carvalho, S. Decorative Chromium Coatings on Polycarbonate Substrate for the Automotive Industry. *Materials* **16**, 2315 (2023).
4. Wint, N., Warren, D., DeVooys, A. & McMurray, H. The use of chromium and chromium (III) oxide PVD coatings to resist the corrosion driven coating delamination of organically coated packaging steel. *J. Electrochem. Soc.* **167**, 141506 (2020).
5. Parsa, Y. et al. Effect of oxygen partial pressure on the semiconducting properties of thermally grown chromia on pure chromium. *Corros. Sci.* **141**, 46–52 (2018).
6. Lozano-Morales, A., Renz, R., Fortman, J. & Taylor, E. Electrically mediated process for functional and decorative trivalent chromium electroplating: an alternative to hexavalent chromium. *ECS Trans.* **6**, 51–61 (2007).
7. Liang, A. & Zhang, J. Why the decorative chromium coating electrodeposited from trivalent chromium electrolyte containing formic acid is darker. *Surf. Coat. Technol.* **206**, 3614–3618 (2012).
8. Teixeira, L. A. C. & Santini, M. C. Surface conditioning of ABS for metallization without the use of chromium baths. *J. Mater. Process. Technol.* **170**, 37–41 (2005).
9. Pinheiro, X. L. et al. The combination of electrodeposited chromium (III) and PVD as an industrial viable solution for the replacement of electrodeposited chromium (VI). *Process Saf. Environ. Prot.* **182**, 727–739 (2024).
10. Christoforou, P., Dowding, R., Pinna, C. & Lewis, R. Two-layer laser clad coating as a replacement for chrome electroplating on forged steel. *P I Mech. Eng. C-j. Mec.* **235**, 7120–7138 (2021).
11. Wang, Q., Luo, S., Wang, S., Wang, H. & Ramachandran, C. S. Wear, erosion and corrosion resistance of HVOF-sprayed WC and Cr₃C₂ based coatings for electrolytic hard chrome replacement. *Int. J. Refract. Met. Hard Mater.* **81**, 242–252 (2019).
12. Safavi, M. S. & Rasooli, A. The positive contribution of Cr₂O₃ reinforcing nanoparticles to enhanced corrosion and tribomechanical performance of Ni–Mo alloy layers electrodeposited from a citrate-sulfate bath. *J. Mater. Res Technol.* **28**, 865–878 (2024).

13. Agüero, A. et al. HVOF-Deposited WCCoCr as Replacement for Hard Cr in Landing Gear Actuators. *J. Therm. Spray. Technol.* **20**, 1292–1309 (2011).
14. Navinšek, B., Panjan, P. & Milošev, I. PVD coatings as an environmentally clean alternative to electroplating and electroless processes. *Surf. Coat. Technol.* **116–119**, 476–487 (1999).
15. Legg, K. O. et al. The replacement of electroplating. *Surf. Coat. Technol.* **81**, 99–105 (1996).
16. Martinuzzi, S. et al. A Comparative Research on Corrosion Behavior of Electroplated and Magnetron Sputtered Chromium. *Coat. Coat.* **12**, 257 (2022).
17. Wang, S., Miao, Y. & Si, C. A novel CrCx/C-Cr multilayer PVD coating for cotton picking spindle: Committed to replacing traditional electroplated chromium coating. *Phys. Scr.* **99**, 025016 (2024).
18. He, J. et al. Modification of Cr/CrN composite structure by Fe addition and its effect on decorative performance and corrosion resistance. *Ceram. Int.* **47**, 23888–23894 (2021).
19. Wu, J. et al. High vacuum arc ion plating Cr film for promoting high temperature applicability of Cu. *Corros. Sci.* **207**, 110575 (2022).
20. Wang, Z. et al. Comparative study on protective Cr coatings on nuclear fuel cladding Zirlo substrates by AIP and HiPIMS techniques. *Ceram. Int.* **49**, 22736–22744 (2023).
21. Mutyala, K. C., Ghanbari, E. & Doll, G. L. Effect of deposition method on tribological performance and corrosion resistance characteristics of Cr_xN coatings deposited by physical vapor deposition. *Thin Solid Films* **636**, 232–239 (2017).
22. Kouznetsov, V., Macák, K., Schneider, J. M., Helmersson, U. & Petrov, I. A novel pulsed magnetron sputter technique utilizing very high target power densities. *Surf. Coat. Technol.* **122**, 290–293 (1999).
23. Hecimovic, A. & Ehiasarian, A. Time evolution of ion energies in HIPIMS of chromium plasma discharge. *J. Phys. D: Appl. Phys.* **42**, 135209 (2009).
24. Helmersson, U., Lättemann, M., Bohlmark, J., Ehiasarian, A. P. & Gudmundsson, J. T. Ionized physical vapor deposition (IPVD): A review of technology and applications. *Thin Solid Films* **513**, 1–24 (2006).
25. Zhang, D. et al. Comparative study on protective properties of CrN coatings on the ABS substrate by DCMS and HiPIMS techniques. *Surf. Coat. Technol.* **394**, 125890 (2020).
26. Kuo, C.-C., Lin, C.-H., Lin, Y.-T. & Chang, J.-T. Effects of Cathode Voltage Pulse Width in High Power Impulse Magnetron Sputtering on the Deposited Chromium Thin Films. *Coatings* **10**, 542 (2020).
27. Han, Z. et al. Tailored high-temperature corrosion behavior of Cr coatings using high power impulse magnetron sputtering on ZIRLO alloys for accident-tolerant fuel application. *Surf. Coat. Technol.* **488**, 130941 (2024).
28. Wang, D. et al. Sand erosion and crack propagation mechanism of Cr/CrN/Cr/CrAlN multilayer coating. *Ceram. Int.* **48**, 24638–24648 (2022).
29. Ibrahim, K. et al. Annealing effects on microstructural, optical, and mechanical properties of sputtered CrN thin film coatings: Experimental studies and finite element modeling. *J. Alloy. Compd.* **750**, 451–464 (2018).
30. Mydlowska, K., Myśliński, P., Szparaga, Ł., Gilewicz, A. & Jerzy, R. Analysis of the effect of antiwear CrN coating thickness on the evolution of thermomechanical interactions in the substrate/PVD coating system. *J. Therm. Anal. Calorim.* **125**, 1241–1247 (2016).
31. Zeilinger, A. et al. Resolving depth evolution of microstructure and hardness in sputtered CrN film. *Thin Solid Films* **581**, 75–79 (2015).
32. Zhang, F., Yan, M., He, J. & Yin, F. Microstructures and nano-mechanical properties of multilayer coatings prepared by plasma nitriding Cr-coated Al alloy. *Vacuum* **142**, 106–113 (2017).
33. Conrad, H. Effect of interstitial solutes on the strength and ductility of titanium. *Prog. Mater. Sci.* **26**, 123–403 (1981).
34. Tyson, W. R. Strengthening of hcp Zr, Ti and Hf by interstitial solutes – a review. *Can. Metall. Q.* **6**, 301–332 (1967).
35. Mouawad, B., Boulnat, X., Fabrègue, D., Perez, M. & de Carlan, Y. Tailoring the microstructure and the mechanical properties of ultrafine grained high strength ferritic steels by powder metallurgy. *J. Nucl. Mater.* **465**, 54–62 (2015).
36. Firstov, S. O., Rohul', T. H., Svechnikov, V. L. & Dub, S. M. Concept of “useful” impurities and mechanical properties of nanostructured chromium and molybdenum films. *Mater. Sci.* **42**, 121–126 (2006).
37. Lei, Z. et al. Enhanced strength and ductility in a high-entropy alloy via ordered oxygen complexes. *Nature* **563**, 546–550 (2018).
38. Erdemir, A. A crystal chemical approach to the formulation of self-lubricating nanocomposite coatings. *Surf. Coat. Technol.* **200**, 1792–1796 (2005).
39. Xu, J., Cheng, J., Jiang, S., Munroe, P. & Xie, Z.-H. The influence of Ti additions on the mechanical and electrochemical behavior of β -Ta₅Si₃ nanocrystalline coating. *Appl. Surf. Sci.* **419**, 901–915 (2017).
40. Yuan, L. & Wang, H. M. Corrosion behaviors of a γ -toughened Cr₁₃Ni₅Si₂/Cr₃Ni₅Si₂ multi-phase ternary metal silicide alloy in NaCl solution. *Electrochim. Acta* **54**, 421–429 (2008).
41. Zheng, X., Castaneda, H., Gao, H. & Srivastava, A. Synergistic effects of corrosion and slow strain rate loading on the mechanical and electrochemical response of an aluminium alloy. *Corros. Sci.* **153**, 53–61 (2019).
42. Li, X. et al. Improvement of corrosion resistance of H59 brass through fabricating superhydrophobic surface using laser ablation and heating treatment. *Corros. Sci.* **180**, 109186 (2021).
43. Chidambaram, D., Clayton, C. R. & Dorfman, M. R. Evaluation of the electrochemical behavior of HVOF-sprayed alloy coatings. *Surf. Coat. Technol.* **176**, 307–317 (2004).
44. dos Santos, A. M. M. et al. Corrosion and cell viability studies of graphite-like hydrogenated amorphous carbon films deposited on bare and nitrided titanium alloy. *Corros. Sci.* **82**, 297–303 (2014).
45. Liu, Y. et al. Controllable defect engineering to enhance the corrosion resistance of Cr/GLC multilayered coating for deep-sea applications. *Corros. Sci.* **199**, 110175 (2022).
46. Matthes, B. et al. Corrosion performance of some titanium-based hard coatings. *Surf. Coat. Technol.* **49**, 489–495 (1991).
47. Tsuchiya, H., Fujimoto, S., Chihara, O. & Shibata, T. Semiconductive behavior of passive films formed on pure Cr and Fe–Cr alloys in sulfuric acid solution. *Electrochim. Acta* **47**, 4357–4366 (2002).
48. Cardoso, M. V., Amaral, S. T. & Martini, E. M. A. Temperature effect in the corrosion resistance of Ni–Fe–Cr alloy in chloride medium. *Corros. Sci.* **50**, 2429–2436 (2008).
49. Wang, Z. et al. Recent research progress on the passivation and selective oxidation for the 3d-transition-metal and refractory multi-principal element alloys. *NPJ Mater. Degrad.* **7**, 86 (2023).
50. Rigter, S. A. et al. Passivation Properties and Formation Mechanism of Amorphous Halide Perovskite Thin Films. *Adv. Funct. Mater.* **31**, 2010330 (2021).
51. Zheng, Z. B., Zheng, Y. G., Sun, W. H. & Wang, J. Q. Effect of applied potential on passivation and erosion–corrosion of a Fe-based amorphous metallic coating under slurry impingement. *Corros. Sci.* **82**, 115–124 (2014).
52. Zhang, Z.-C., Lan, A.-D., Zhang, M. & Qiao, J.-W. Effect of Ce on the pitting corrosion resistance of non-equiatomic high-entropy alloy Fe₄₀Mn₂₀Cr₂₀Ni₂₀ in 3.5 wt% NaCl solution. *J. Alloy. Compd.* **909**, 164641 (2022).

Acknowledgements

This research was supported by the National Natural Science Foundation of China (52171090), the National Science Fund for Distinguished Young Scholars of China (52025014), Key Research and Development Program of Ningbo (2023Z110), and the Natural Science Foundation of Ningbo (2023QL049).

Author contributions

M.Z.: Conceptualization, Methodology Investigation, Formal Analysis, Validation and Writing-Original. L.W.: Validation. Z.W.: Methodology, Validation. Y.C.: Software. G.M.: Methodology Investigation. S.T.: Writing-Review & Editing. P.K.: Validation, Editing, Funding Acquisition. A.W.: Writing-Review & Editing, Funding Acquisition, Supervision. All authors reviewed the manuscript.

Competing interests

The authors declare no competing interests.

Additional information

Correspondence and requests for materials should be addressed to Zhenyu Wang or Aiying Wang.

Reprints and permissions information is available at <http://www.nature.com/reprints>

Publisher's note Springer Nature remains neutral with regard to jurisdictional claims in published maps and institutional affiliations.

Open Access This article is licensed under a Creative Commons Attribution-NonCommercial-NoDerivatives 4.0 International License, which permits any non-commercial use, sharing, distribution and reproduction in any medium or format, as long as you give appropriate credit to the original author(s) and the source, provide a link to the Creative Commons licence, and indicate if you modified the licensed material. You do not have permission under this licence to share adapted material derived from this article or parts of it. The images or other third party material in this article are included in the article's Creative Commons licence, unless indicated otherwise in a credit line to the material. If material is not included in the article's Creative Commons licence and your intended use is not permitted by statutory regulation or exceeds the permitted use, you will need to obtain permission directly from the copyright holder. To view a copy of this licence, visit <http://creativecommons.org/licenses/by-nc-nd/4.0/>.

© The Author(s) 2025